

Pylon-Based Jet Noise Suppressors

Dimitri Papamoschou*

University of California, Irvine, Irvine, California 92697-3975

DOI: 10.2514/1.37780

This experimental investigation examined the potential of pylon-based deployable flaps to reduce jet noise of separate-flow turbofan engines with a bypass ratio of eight. The main function of the flap deflectors is to thicken the low-speed region surrounding the core jet in the downward and sideline directions. The study encompassed acoustic measurements, noise-source imaging, mean-velocity surveys, and aerodynamic estimates. Three types of deflectors were tested: solid flaps, porous flaps made of coarse perforation, and porous flaps made of fine perforation. It is shown that all the deflectors reduce noise sources near the end of the primary potential core. However, the solid flaps create excess noise in the vicinity of their location that can overwhelm this noise benefit, particularly at large polar angles. Porous flaps significantly reduce velocity gradients that cause excess noise. Noise generation from the perforations themselves can be shifted to very high frequency (rapidly attenuated by atmospheric absorption) by reducing the size of the perforation. Accordingly, the fine-perforation flaps provided superior acoustic results yielding effective perceived noise level benefits of 2.1 dB in the downward direction and 1.0 dB in the sideline direction. The static-thrust loss of these flaps is estimated at 0.7%.

Nomenclature

A	=	nozzle area
C_p	=	pressure coefficient
c	=	flap chord length
D_f	=	fan nozzle exit diameter
D_{flap}	=	flap drag
F	=	thrust
f	=	frequency
h	=	flap height
h_e	=	fan nozzle exit height
r	=	radial coordinate
S	=	autospectrum of acoustic pressure
St	=	Strouhal number
U_p	=	primary (core) exit velocity
U_s	=	secondary (fan) exit velocity
u	=	axial mean velocity
x	=	axial coordinate from exit of core nozzle
y	=	transverse coordinate on symmetry plane
z	=	transverse coordinate normal to symmetry plane
α	=	flap angle
θ	=	polar angle from jet axis
ρ_s	=	density of exit fan flow
ϕ	=	azimuth angle measured from downward vertical
Ψ	=	noise-source distribution

I. Introduction

FAN flow deflection is a directional noise suppression method applicable to separate-flow turbofan engines [1,2]. The deflectors thicken the low-speed flow underneath the core jet, resulting in lower noise emission toward the ground. The diagram of Fig. 1 describes principal features of the mean flowfield of a coaxial jet thought to play a role in noise emission [2]. The primary core (PC) is defined as the region where the velocity exceeds a high threshold, typically 80% of the core exit velocity, and represents the region of the most intense noise sources. The secondary core (SC) is defined by

Presented as Paper 40 at the 46th AIAA Aerospace Sciences Meeting and Exhibit, Reno, NV, 7–10 January 2008; received 28 March 2008; revision received 27 October 2008; accepted for publication 30 October 2008. Copyright © 2008 by D. Papamoschou. Published by the American Institute of Aeronautics and Astronautics, Inc., with permission. Copies of this paper may be made for personal or internal use, on condition that the copier pay the \$10.00 per-copy fee to the Copyright Clearance Center, Inc., 222 Rosewood Drive, Danvers, MA 01923; include the code 0001-1452/09 \$10.00 in correspondence with the CCC.

*Professor, Department of Mechanical and Aerospace Engineering, 4200 Engineering Gateway. Fellow AIAA.

the outer inflection points i_2 and i_3 of the radial velocity profile, which naturally form a loop. For typical fan-to-core velocity ratios in turbofan engines, the primary shear layer (between the core and fan flows) surrounded by the secondary core makes a negligible contribution to sound emission [2,3]. This ability of the secondary flow to silence the primary shear layer is the foundation of noise-reduction concepts that extend the secondary core (via offset nozzles or deflectors) to cover a greater portion of the primary shear layer that emits downward noise [1,2,4–6].

The present work extends previous concepts of wedge-shaped fan flow deflectors [1,4–6] to wing-mounted turbofan engines incorporating a pylon. This type of engine installation is found in the majority of commercial jet aircraft. The mounting pylon becomes a natural place to attach a wedge or flap that directs the fan flow in the sideward and downward directions. The most practical implementation is thought to be that of a moveable flap, depicted in Fig. 2, deployed during takeoff and retracted for the remainder of the flight. The paper presents acoustic data, mean-velocity distributions, and aerodynamic estimates for the basic configuration shown in Fig. 2 and some variants. The nozzle has the flow lines of the NASA John H. Glenn Research Center's (GRC) 5BB (baseline) nozzle [5] with a bypass ratio of eight.

The advent of nonaxisymmetric nozzle concepts for jet noise suppression led to large-scale tests at GRC under the program entitled Offset Stream Technologies. Configurations included internal vanes and internal wedge deflectors [5]. The overall agreement with the small-scale data on vanes, obtained at the University of California, Irvine (UCI), was good. However, the GRC wedges aggressively deflected the flow and suffered from excessive noise in the 90-deg polar direction, which reduced their acoustic benefit. There are two likely causes of the excess noise: high-velocity gradients in the primary shear layer due to the lack of secondary flow in the wake of the wedge, and deflector self-noise, that is, sound generation due to turbulence in the wake of the wedge. The generation of strong velocity gradients, and resulting large values of the turbulent kinetic energy, in the vicinity of the wedge are evident in the experimental measurements of Shupe et al. [6]. The present study will show that both noise sources can play a significant role in the acoustic performance of wedge-type deflectors. Importantly, the magnitude of both sources can be reduced by proper design of the deflector.

II. Experimental Setup

A. Nozzle and Flow Conditions

The nozzle used is a one-eighth scale version of the bypass ratio (BPR) 8 nozzle used at GRC (5BB nozzle). The nozzle coordinates

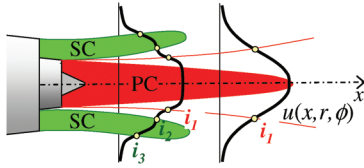


Fig. 1 Principal features of mean-velocity field in a coaxial jet with regard to noise generation.

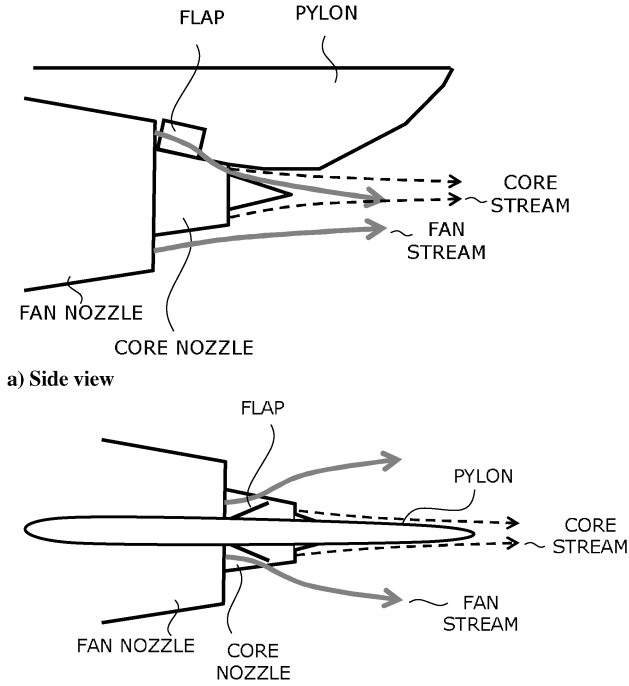


Fig. 2 Basic concept of pylon-mounted jet noise suppressor.

are shown Fig. 3. The fan exit diameter is $D_f = 31.2$ mm, and the fan exit height is $h_e = 4$ mm. Exit conditions are listed in Table 1 for the acoustic tests and mean-velocity surveys. The acoustic tests used helium-air mixtures to match the velocities and Mach numbers of a BPR = 8 engine cycle at takeoff thrust. Use of helium-air mixtures for mean-velocity surveys is prohibitive because the tests are very long and would consume inordinate amounts of helium. For this reason, the mean-velocity surveys used pure air supplied by compressors. Even though the velocities were lower than those of a realistic turbofan exhaust (used in the acoustic tests), the velocity ratio of 0.77 matched the velocity ratio in the acoustics tests. By matching the velocity ratio, it is hoped to preserve the principal fluid mechanic of shear-layer mixing. Of course, we miss the effect of elevated temperature (lower density) of the core stream, which is

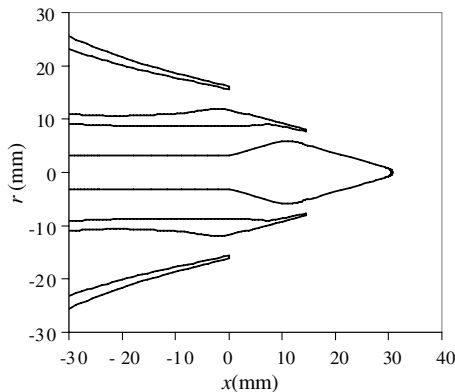


Fig. 3 Nozzle coordinates.

Table 1 Exhaust conditions

	Acoustic tests		Mean flow surveys	
	Core	Fan	Core	Fan
Velocity, m/s	390	300	285	217
Mach no.	0.72	0.86	0.90	0.66

expected to produce a shorter primary potential core. Recent experiments indicate that the mean-velocity fields of cold and hot jets collapse once the axial distance is normalized by the potential-core length [7]. Therefore, it is anticipated that the mean-flow trends found here will apply to heated jets qualitatively, and possibly quantitatively, with proper scaling of the axial coordinate. Finally, it is noted that the facility does not have capability of external flow, therefore all the data shown here are for static conditions.

The Reynolds number of the jet, based on fan diameter, was 6.8×10^5 for the acoustic tests and 5.4×10^5 for the mean-flow surveys. Both values exceeded the criterion of 4×10^5 suggested by Viswanathan [8] for avoiding effects of low Reynolds number. For the acoustic tests, the Reynolds numbers based on annulus exit heights of the core and fan nozzles were 87,000 and 40,000, respectively. Based on these values, and the rapid acceleration of the flow near the nozzle exit, it is expected that the boundary layers were laminar. An extensive investigation of jet noise data by Viswanathan [8] indicates that the state of the boundary layer (laminar or turbulent) has no impact on the radiated noise.

Past works have shown that small-scale, helium-air mixture jets duplicate accurately the acoustics of large-scale hot jets using the same nozzle flow lines. Figure 4 shows a comparison of sound pressure level spectra for the 5BB baseline nozzle between the UCI facility (small-scale, helium-air mixture jets) and the GRC facility (large-scale, hot jets).

B. Pylon

The pylon design is based on the NASA Langley design used in computational and experimental studies of high-bypass nozzles [9]. A special feature of the UCI pylon used in this study is the incorporation of slots along which one can slide inserts with various flap deflectors, as shown in Fig. 5. One pair of inserts was clean (without deflectors), thus forming the baseline pylon. This arrangement enabled the study of various deflectors without having to disassemble the nozzle or the pylon, thus enhancing the accuracy of the noise reductions recorded. This point is further discussed in Sec. II.D.

C. Pylon Flaps

The flap design used here had an angle $\alpha = 22$ deg (this corresponds to the wedge half-angle of previous investigations), length of 10 mm ($2.5h_e$), and height of 5 mm ($1.25h_e$). This was thought to be a reasonable design for practical implementation; however, it was

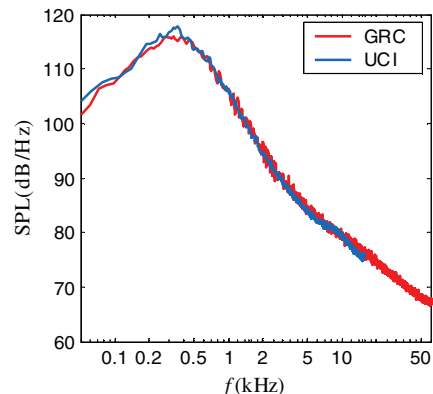


Fig. 4 Comparison of UCI and GRC spectra for 5BB nozzle at polar angle $\theta = 30$ deg. Data from [5].

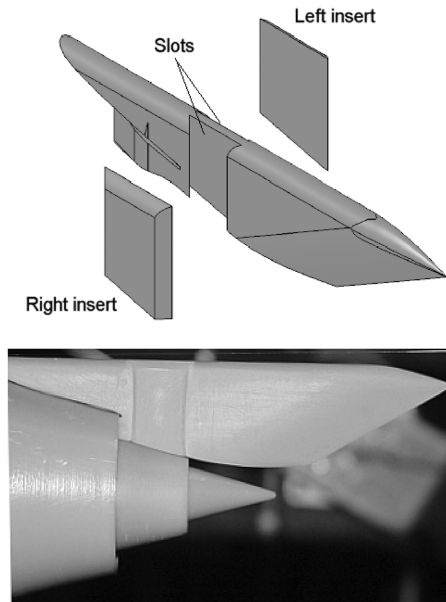


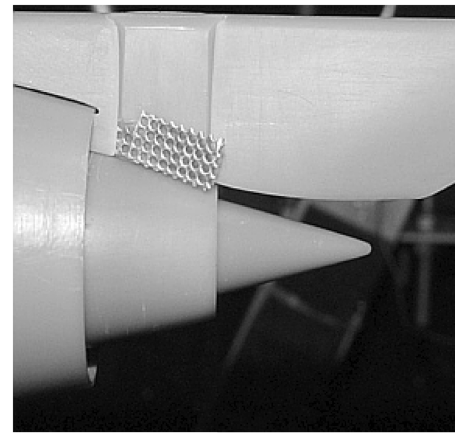
Fig. 5 Pylon design with slot inserts.

not the result of any optimization. The flap material reflected the desire to allow some secondary flow over the top of the core jet to prevent creation of strong velocity gradients. Two types of perforations, coarse and fine, were tried, as listed in Table 2. Both types of perforated flaps had roughly the same open area ($\sim 50\%$). Solid flaps were created by attaching transparent adhesive tape of 0.05-mm thickness over the perforated sheet. Figure 6 shows the two types of perforated flaps used. The perforation designs were restricted by materials that were readily available commercially. Future research will use custom-made perforations with designs influenced by the findings of this investigation.

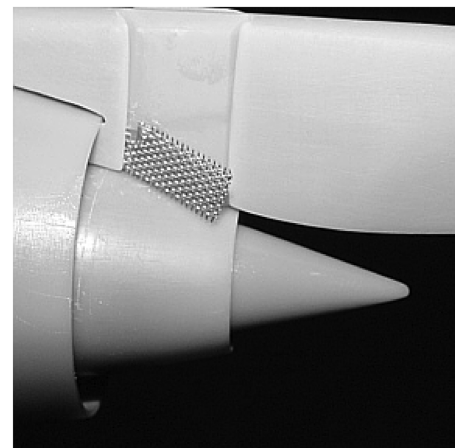
D. Noise Measurement

The nozzle was attached to a dual-stream apparatus delivering cold mixtures of helium and air to the primary (core) and secondary (bypass) nozzles [1]. The exit flow conditions, listed in Table 1, matched the typical exit conditions of a turbofan engine with bypass ratio 8.0 at takeoff power. Aeroacoustic investigation was performed in the facility shown in Fig. 7. Sound was measured by a microphone array consisting of eight 3.2-mm condenser microphones (Bruel & Kjaer, Model 4138) arranged on a circular arc centered at the vicinity of the nozzle exit. The polar aperture of the array is 30 deg and the array radius is 1 m. The angular spacing of the microphones is logarithmic. The entire array structure is rotated around its center to place the array at the desired polar angle. Positioning of the array is done remotely using a stepper motor. An electronic inclinometer displays the polar angle of the first microphone. Measurements at various azimuth angles are enabled by rotating the nozzle around its axis. Figure 7 illustrates the definitions of polar angle θ and azimuth angle ϕ used in this paper.

The microphones are connected, in groups of four, to two amplifier/signal conditioners (Bruel & Kjaer, Model 2690-A-OS4) with high-pass filter set at 300 Hz and low-pass filter set at 100 kHz. The four-channel output of each amplifier was sampled at 250 kHz per channel by a multifunction data acquisition board (National Instruments PCI-6070E). Two such boards, one for each amplifier, are installed in a Pentium 4 personal computer. National Instruments LabView software is used to acquire the signals. The sound pressure



a) Coarse perforation



b) Fine perforation

Fig. 6 Installation of pylon flaps.

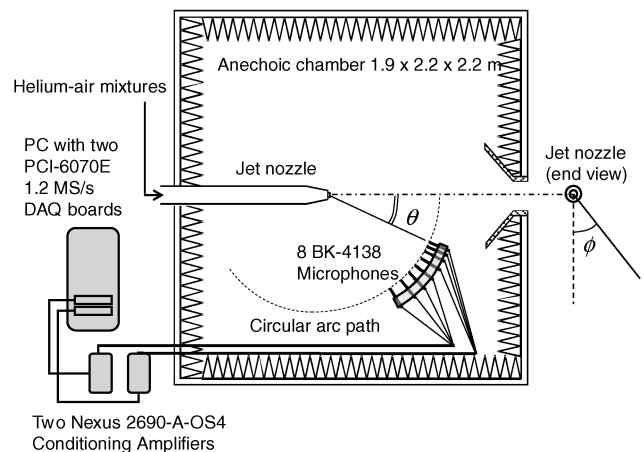


Fig. 7 Setup for aeroacoustic testing.

level spectrum was corrected for actuator response, free-field correction, and atmospheric absorption. The overall sound pressure level (OASPL) was obtained by integrating the corrected spectrum. Spectra and OASPL are referenced to a distance of $1.25 D_f$ from the nozzle exit.

Table 2 Flap construction

Designation	Material	Porosity	Hole size	Hole spacing
Solid	Perforated sheet + tape	0.00	—	—
Coarse perforation	Perforated sheet	0.45	0.97 mm	1.27 mm
Fine perforation	Woven mesh	0.49	0.48×0.27 mm	0.63×0.42 mm

The calculation of perceived noise level (PNL) and effective perceived noise level (EPNL) is based on the following: flyover altitude of 457 m and Mach number of 0.2, engine angle of attack of 10 deg, and engine static thrust of 111 kN (25,000 lb). Details of the PNL and EPNL calculation procedure can be found in [1]. Because the acoustic tests are static, the PNL and EPNL predictions do not include the effect of forward flight except in accounting for the Doppler shift of the moving sources.

The repeatability of noise-reduction measurements in dual-stream jets is strongly influenced by the ability to maintain exactly the same baseline nozzle geometry from one test to the next. Past studies have shown significant sensitivity of the flowfield and acoustics to small misalignments in the nozzles that form the primary and secondary streams [10]. Every time a nozzle is reassembled, there is risk of small departures from its previous position. The pylon inserts described in Sec. II.C enabled configuration changes, for a given measurement azimuth angle, without disturbing the nozzle or pylon which were carefully aligned. Changing the measurement azimuth angle required rotation and realignment of the nozzle and pylon. A new baseline measurement (with plain pylon) was obtained every time the nozzle was rotated, and the subsequent tests with pylon flaps were referenced to this baseline. The experiments presented here required two baseline measurements at $\phi = 0$ deg and two baseline measurements at $\phi = 60$ deg. For each azimuth angle, the baselines did not differ by more than 0.1 EPNdB. Further, the case with fine-perforation flaps was tested twice and yielded EPNL estimates differing by only 0.1 dB (the least noise reduction is quoted in this paper). Even though the repeat tests were not extensive, due to resource limitations, the aforementioned findings indicate that the repeatability of the noise-reduction measurements is approximately ± 0.1 EPNdB.

Imaging of the noise sources used the beamforming method described in Papamoschou [11]. The method follows the basic steps of the Deconvolution Approach for the Mapping of Acoustic Sources deconvolution method developed by Brooks and Humphreys [12]; however, the inversion algorithm is different and a directional formulation for the noise source is used. In this paper, the noise-source maps are plotted in a differential form that shows the changes from the baseline.

E. Mean-Velocity Measurement

For the mean-velocity measurements, the nozzles were attached to a duplicate dual-stream apparatus supplying compressed air at room temperature to both the primary (core) and secondary (bypass) streams. The exit conditions are listed in Table 1. The mean-velocity field in the jet plume was measured using a pitot rake system, shown in Fig. 8. The rake consists of five probes of 1.0-mm internal diameter, 70-mm length, and spacing of 10 mm. Each probe is connected individually to a Setra Model 207 pressure transducer. Mounted on a three-dimensional motorized traverse, the rake translated along a preprogrammed path consisting of 14 axial (x) planes spaced apart by 12.7 mm. On each axial plane, the rake swept the jet flow along a reciprocating pattern in y , the z position being

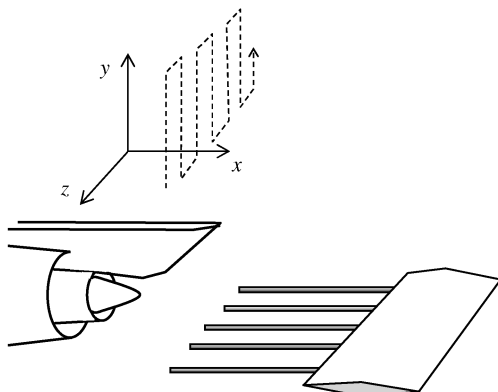


Fig. 8 Setup for mean-velocity surveys.

incremented by 2.5 mm after each y stroke. This pattern is illustrated by the dashed line of Fig. 8. The speed of the y movement was 10 mm/s and was selected carefully after evaluating the time-response of the pitot rake system by traversing at different speeds and ensuring that the details of the velocity profile matched those measured when traversing at very low speed. The pitot pressure was sampled at a rate of 1000 Hz by an analog-to-digital data acquisition board (National Instruments PCI-MIO-16E). This high acquisition rate provided a large number of points for accurate smoothing of the profiles.

The pressure measurements on each axial plane were interpolated on a fixed y - z grid. Mach number and velocity fields were computed from the pitot measurements under the assumptions of constant static pressure (equal to ambient pressure) and constant total temperature (equal to room temperature). Smoothing of the velocity profiles and computation of the velocity gradients was performed using a Savitzky–Golay filter [13].

Some pitot probe surveys were conducted in the vicinity of the pylon flaps, where flow deflections are significant. The maximum deflection angle is the flap angle itself (22 deg), and, downstream of the flap, deflections are much less. Pitot probes have been shown to give 1% accuracy up to yaw angles of 20 deg [14], and so it is expected that the near-field measurements accurately represent the local axial velocity field.

III. Acoustic Results

This section presents two types of acoustic results: single-microphone acoustics, which means data that did not involve cor-

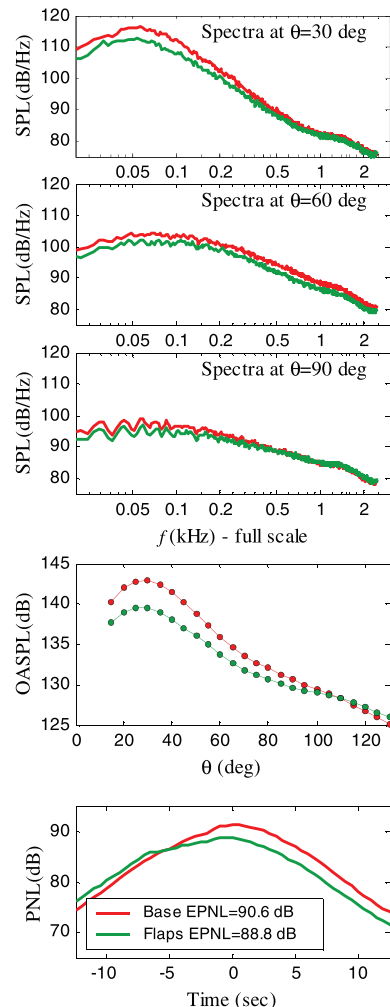


Fig. 9 Acoustic summary for solid flaps. Microphone azimuth $\phi_{mic} = 0$ deg, Δ EPNL = -1.8 dB.

relations between the array microphones, and noise-source maps that were derived from cross-correlating the microphone signals.

A. Single-Microphone Acoustics

For each pylon-flap configuration we present an “acoustic summary” comprising the following quantities: narrowband sound pressure level (SPL) lossless spectra, scaled to full-scale frequency (scale factor of 50), at selected polar angles; directivity of OASPL; PNL versus time; and estimate of EPNL. These quantities are compared against their respective baseline values (red curves). We begin with the acoustic summary for the solid flaps, shown in Figs. 9 and 10 for $\phi_{\text{mic}} = 0$ deg (downward) and 60 deg (sideline), respectively. For $\phi_{\text{mic}} = 0$ deg, there is acoustic benefit up to $\theta = 100$ deg, above which the spectrum shows a crossover at high frequency. There is a significant EPNL reduction of 1.8 dB. However, for $\phi_{\text{mic}} = 60$ deg, the crossover occurs much earlier, at $\phi_{\text{mic}} = 70$ deg, and the increase in high-frequency sound is more pronounced. This negates the benefits at low polar angles and, as a result, there is an EPNL excess of 0.5 dB. The spectral increases at large polar angles and high frequency are reminiscent of those seen in the offset stream technology tests with internal wedges [5]. As will be shown later, the excess sound is likely due to the strong shear that develops on the top of the core jet as well as velocity gradients caused by the deflector itself. The reason why the 60-deg azimuth is more sensitive to these phenomena may have to do with the “line of sight”

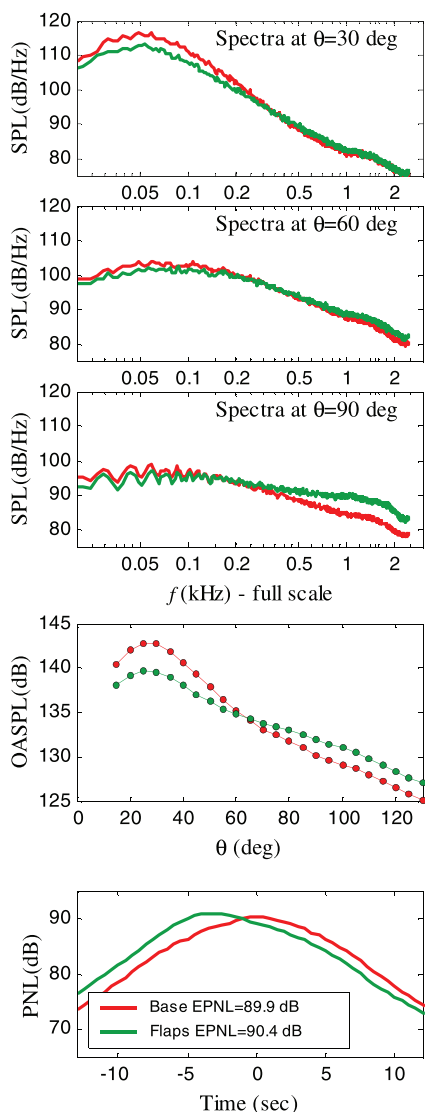


Fig. 10 Acoustic summary for solid flaps. Microphone azimuth $\phi_{\text{mic}} = 60$ deg. $\Delta\text{EPNL} = +0.6$ dB.

of the measurement. Assuming that the high-gradient region is fairly confined to the top of the jet, the observer at $\phi_{\text{mic}} = 0$ sees this region only through refraction by the jet flow, but the observer at $\phi_{\text{mic}} = 60$ has direct line of sight. On the other hand, if the high-gradient region spreads substantially, it will affect observations at all azimuth angles.

The acoustics of the coarse-perforation flaps are shown in Figs. 11 and 12 for $\phi_{\text{mic}} = 0$ deg and 60 deg, respectively. Interestingly, the reductions in peak OASPL are roughly the same as with the solid flaps, even though the perforated flaps have a porosity of 45%. Importantly, the adverse effects of the solid flaps are mitigated. The spectral increases at large polar angles and high frequency are significantly reduced. As a result, the EPNL benefit at $\phi_{\text{mic}} = 0$ deg increases to 2.3 dB. However, a new problem arises: the spectra at high polar angles show a narrowband increase at full-scale frequency of 1.5 kHz. This is particularly strong at $\phi_{\text{mic}} = 60$ deg and practically eliminates the sideline EPNL benefit. Section IV.C discusses the possible physics of this sound generation.

Replacing the coarse perforation with a fine perforation of roughly equal porosity eliminates the problem of deflector self-noise and prevents the creation of strong gradients. It is evident from Figs. 13 and 14 that the fine-perforation flaps provide superior acoustics results and a cumulative EPNL reduction of 3.1 dB, versus 1.5 dB for the solid flaps and 2.5 dB for the coarse-perforation flaps.

The impact of the flap deflectors on noise at $\theta = 100$ deg is further illustrated in the spectral plots of Fig. 15. The figure underscores the dramatic effects that small details in the deflector design can have

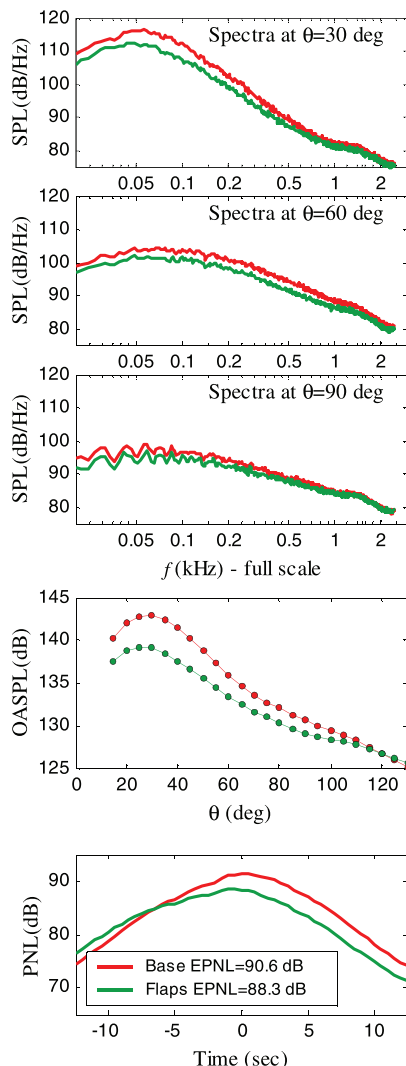


Fig. 11 Acoustic summary for coarse-perforation flaps. Microphone azimuth $\phi_{\text{mic}} = 0$ deg. $\Delta\text{EPNL} = -2.3$ dB.

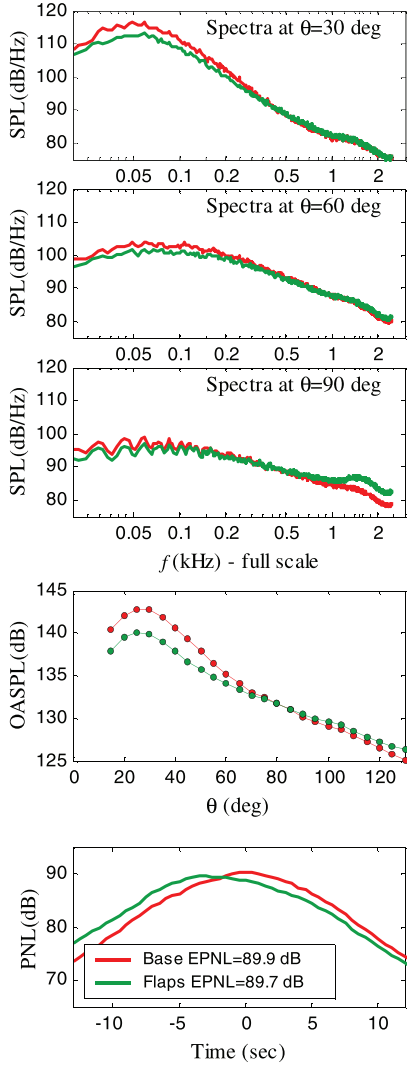


Fig. 12 Acoustic summary for coarse-perforation flaps. Microphone azimuth $\phi_{\text{mic}} = 60$ deg. $\Delta\text{EPNL} = -0.2$ dB.

on the acoustic field. The solid flaps create a region of high gradient (and therefore strong turbulent kinetic energy production), which causes a broadband increase of the sound spectrum. The coarse-perforation flaps allowed some air over the top of the jet and thus prevented the broadband spectral increase, but introduced their own spectral spike. The fine-perforation flaps prevented both effects. Another important realization is that these adverse effects are accentuated when the troublesome source is in the line of sight of the observer, in this case the sideline direction $\phi = 60$ deg.

B. Noise-Source Maps

Cross-correlations of the microphone signals enabled the determination of an axial noise-source distribution $\Psi(\theta, x, f)$. The source imaging procedure [10] allows $\Psi(\theta, x, f)$ to be self-consistent, that is, its axial integration (weighted by the distance factor) gives the autospectrum of the far-field pressure $S(\theta, f)$ for each polar angle surveyed:

$$S(\theta, f) = \int_L \frac{1}{l^2(x)} \Psi(\theta, x, f) dx$$

where $l(x)$ is the distance of the observer from source and L denotes the axial extent of the noise-source region. In this paper, we focus on the changes in the noise-source distribution Ψ caused by the various pylon deflectors and accordingly define the parameter

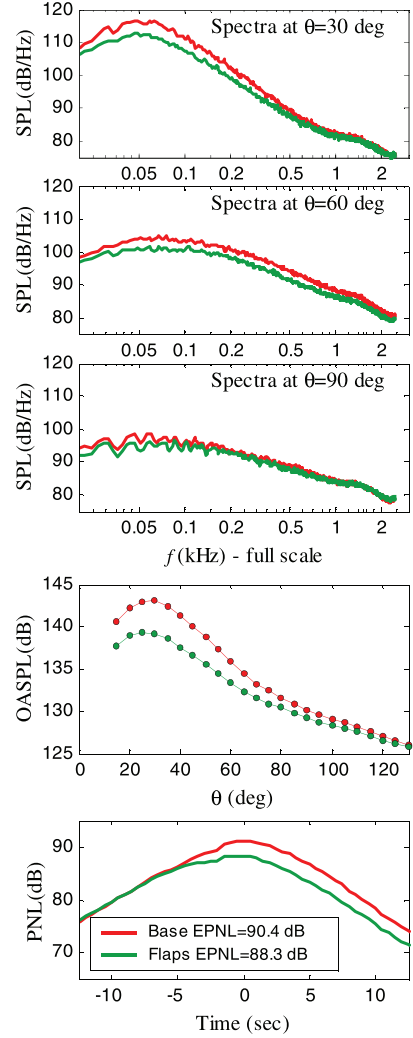


Fig. 13 Acoustic summary for fine-perforation flaps. Microphone azimuth $\phi_{\text{mic}} = 0$ deg. $\Delta\text{EPNL} = -2.1$ dB.

$$\text{noise source reduction} = 100 \frac{\Psi_{\text{base}}(\theta, x, f) - \Psi(\theta, x, f)}{\Psi_{\text{base.max}}(\theta)}$$

where the normalization is done by the global maximum of the baseline noise-source distribution for each polar angle. It is not appropriate to present this type of noise reduction in decibels, hence the presentation is done in a linear scale. Consequently, the dynamic range of the maps is somewhat limited. Negative values of the preceding parameter indicate noise increase. Figures 16 and 17 show contours of the differential noise-source maps for the sideline direction ($\phi = 60$ deg) and for polar angles of 45 and 100 deg, respectively. At $\theta = 45$ deg, all the deflectors act similarly to decrease noise in the low- to midfrequency range. The maximum reduction is centered at $x/D_f = 4-6$, which will be shown later to correspond to the end of the primary potential core. We note that the solid flaps create a slight excess noise source at Strouhal number $Sr \approx 1$ and $x/D_f \approx 0$. We will see that this excess noise, although small at $\theta = 45$ deg, dominates at large polar angles.

At $\theta = 100$ deg, Fig. 17, the solid flaps create relatively strong excess noise near the nozzle exit, which overwhelms the noise benefit that occurs near the end of the potential core. The excess noise is reduced significantly by the perforations. The coarse-perforation flaps, however, create a small noise increase at $Sr \approx 8$ and $x/D_f \approx 0$. This corresponds to the spectral spike of Fig. 15b and is believed to be caused by “jetlets” emerging from the circular perforations, to be discussed in Sec. IV.C. The fine-perforation flaps give the least amount of excess noise. Figures 16 and 17

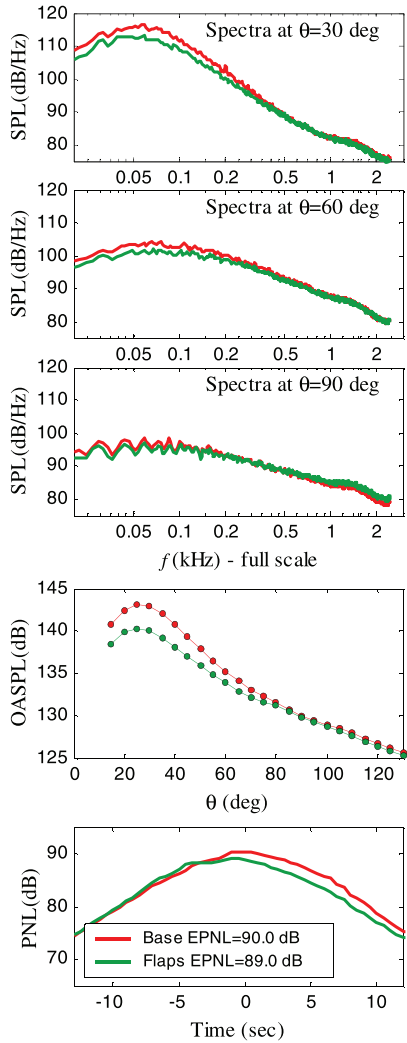


Fig. 14 Acoustic summary for fine-perforation flaps. Microphone azimuth $\phi_{\text{mic}} = 60$ deg. $\Delta\text{EPNL} = -1.0$ dB.

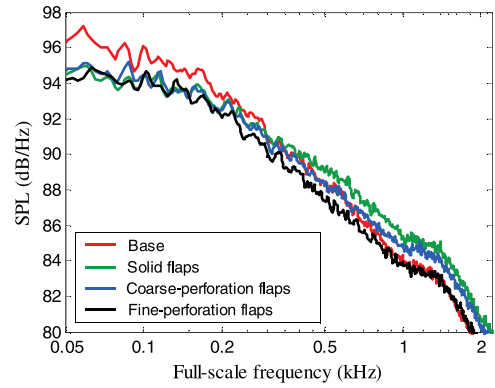
highlight important acoustical aspects of the pylon-flap deflectors. All of them performed their intended function of reducing noise emitted near the end of the potential core. However, the solid flaps created excess noise near the nozzle exit that overwhelmed the noise benefit at large polar angles. The excess noise is believed to be associated with increased shear at the top of the jet. As a result, the sound pressure level spectrum increased, as shown in Fig. 15b. The perforated flaps significantly alleviated this undesirable phenomenon.

IV. Aerodynamics

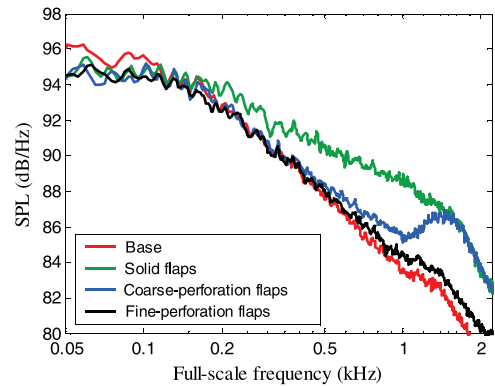
We now discuss aerodynamics aspects of the deflector flaps as they impact thrust loss and sound generation.

A. General Overview

Surface pressure distributions on an external fan flow deflection (FFD) wedge were measured by Papamoschou et al. [15]. Figure 18 summarizes their experimental configuration and key findings. It is assumed that their basic results extend to pylon flaps. There are fundamental differences between the aerodynamics of the FFD wedge and the aerodynamics of the classic, fully-immersed, two-dimensional wedge (i.e., a triangular cylinder). They rise from the fact that the stream on the top side of the wedge is a free surface (edge of the jet) exposed to the ambient pressure. The key differences are as follows.



a) $\phi_{\text{mic}} = 0$ deg



b) $\phi_{\text{mic}} = 60$ deg

Fig. 15 Spectra at $\theta = 100$ deg for baseline and various pylon flaps.

1) A compression develops over the entire side surface of the FFD wedge. As a result, each side of the wedge produces a net lift (side force) that pushes the fan flow away from the wedge. In contrast, in the case of the classic wedge, the pressure over the side surface first increases and then decreases relative to the ambient value. The net lift over each side surface is practically zero. This means that the classic wedge cannot produce a net deflection of the flow far from the wedge (i.e., the streamlines close and form a recirculation region). (This argument does not include diffusion effects that will cause the wake to spread.)

2) The base pressure of the FFD wedge is much less negative than that of the classic wedge. As a result, the drag of the FFD wedge is about 75% less than that of the classic wedge, for a wedge half-angle of 15 deg.

3) Because of the compression over the side of the wedge, the free surface of the fan flow deflects upward, as shown in Fig. 18a. This upwash may have important consequences on excess noise generation to be discussed further in Sec. V.

The differences in the pressure fields are quantified in the pressure coefficient plots of Fig. 18b. For the classic wedge, the pressure coefficient on the side surface is positive near the apex but becomes negative near the base. The base pressure coefficient is $C_{pb} = -0.95$. For the FFD wedge, the side surface develops a uniformly positive C_p with average value of about 0.15, and the base pressure coefficient is $C_{pb} = -0.20$. These results are fairly insensitive to the jet Mach number.

To estimate the effect of perforations on drag created by the flaps, we use the results of Castro [16] who studied the wake characteristics of two-dimensional perforated plates normal to an airstream. Although Castro's geometry and flowfield are different from ours, it is assumed that the relative reduction in drag due to porosity applies to the FFD perforated flaps. According to Castro's data, increasing the porosity from 0 to 50% reduces the drag by approximately 50%.

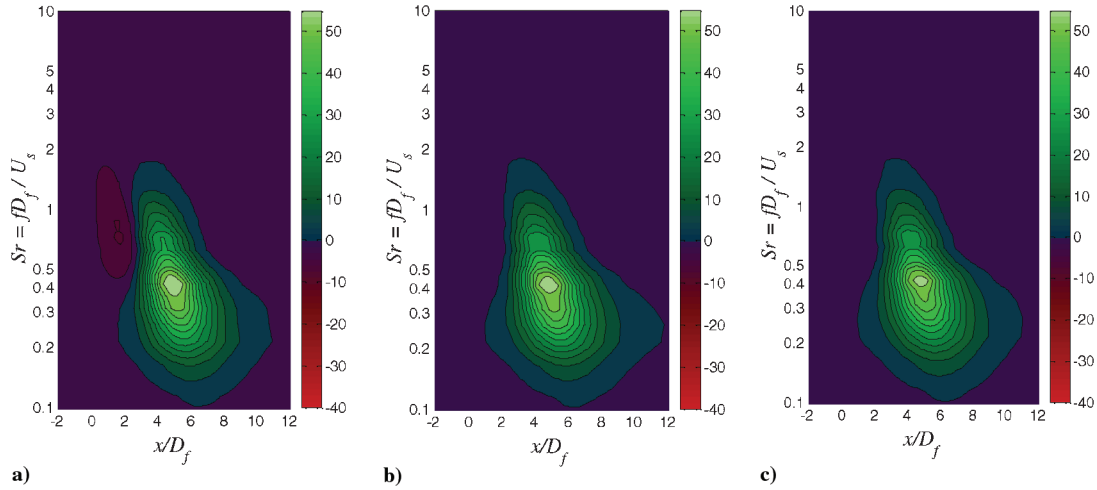


Fig. 16 Noise-source reduction maps for $\theta = 45$ deg and $\phi = 60$ deg: a) solid flaps, b) coarse-perforation flaps, and c) fine-perforation flaps.

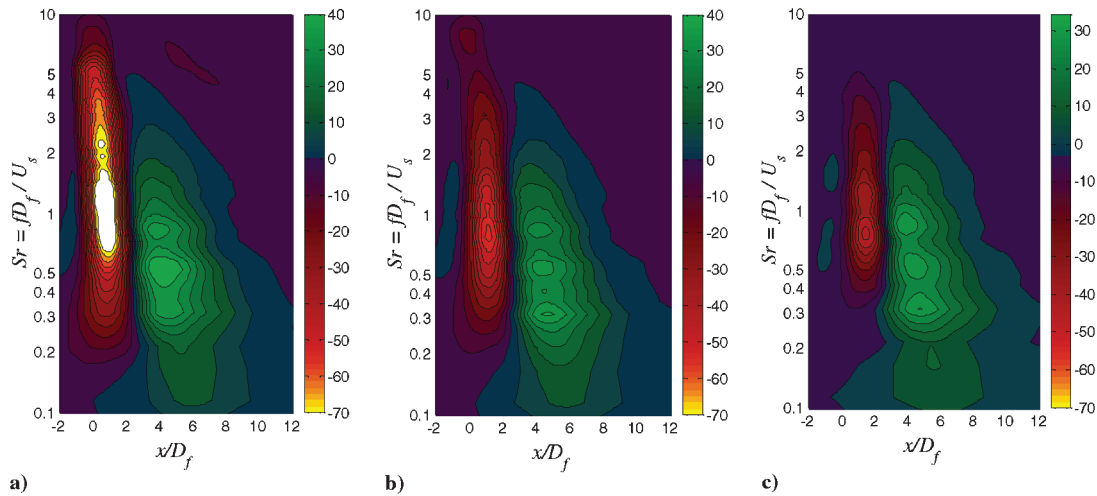


Fig. 17 Noise-source reduction maps for $\theta = 100$ deg and $\phi = 60$ deg: a) solid flaps, b) coarse-perforation flaps, and c) fine-perforation flaps.

B. Drag Estimate

In the aerodynamics experiments of [15], each half of the wedge was treated like an airfoil producing lift (side force) and drag. The sectional lift and drag coefficients were based on the chord length c of the wedge. Assuming that their finding also extend to flaps, the drag of a pair of flaps is

$$D_{\text{flap}} = 2C_{D\frac{1}{2}}\rho_s U_s^2 hc$$

The static thrust of the secondary (fan) stream is

$$F_s = \rho_s U_s^2 A_s$$

thus,

$$\frac{D_{\text{flap}}}{F_s} = C_D \frac{hc}{A_s}$$

For the dimensions of the 5BB nozzle and current flaps,

$$\frac{D_{\text{flap}}}{F_s} = 0.12C_D$$

According to Papamoschou et al. [15], for a wedge with half-angle $\alpha = 15$ deg, the drag coefficient at nozzle pressure ratio NPR = 1.6 is 0.063. Here, we assume that C_D scales with α^2 , and so for $\alpha = 22$ deg we get $C_D = 0.135$ for the solid flaps. For the perforated flaps, with porosity of 50%, the drag coefficient is expected to drop by 50% to $C_D = 0.067$. The thrust loss of the fan stream is therefore 1.6% with the solid flaps and 0.8% for the perforated flaps.

Considering that the fan stream delivers 86% of the total thrust, the thrust loss for the entire engine is 1.4% for the solid flaps and 0.7% for the perforated flaps. It is emphasized that the flaps would be retractable, and so this penalty would occur only for the takeoff portion of the flight.

C. Sound Generation

In an effort to understand the spectral increase caused by the coarse perforation (Fig. 15b), it is assumed that the self-noise of the perforated flap is primarily due to the jetlets emerging from the perforations. A similar argument can be found in the study of perforated drag plates by Sakaliyski et al. [17]. The velocity of each jetlet depends on the pressure difference between the front and back sides of the flap. It is easy to show that the jetlet velocity is given by

$$u_j = U_s \sqrt{C_{\text{Pf}} - C_{\text{Pb}}}$$

where C_{Pf} and C_{Pb} are average values of the pressure coefficients on the front and back surfaces of the flap, respectively. Now we assume that the pressure coefficient on the front side of the flap scales linearly with flap angle α . Scaling the result of Fig. 18b to $\alpha = 22$ deg gives $C_{\text{Pf}} = 0.2$. It will be shown in the next section that the base pressure coefficient of the perforated flap is practically zero. For $C_{\text{Pf}} = 0.2$, $C_{\text{Pb}} = 0$, and $U_s = 300$ m/s, we obtain $u_j = 140$ m/s. In terms of lab-scale frequency, the coarse perforation caused a spectral peak at $f = 75$ kHz. The corresponding Strouhal number for hole size $d_j = 0.96$ mm is

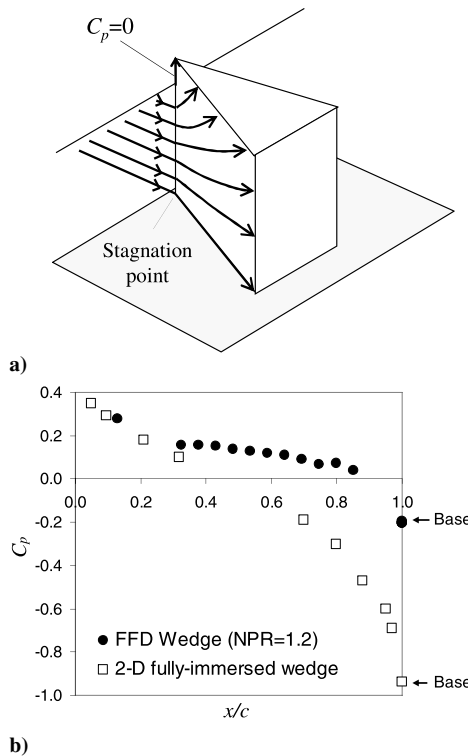


Fig. 18 Experiments on FFD wedge: a) streamline pattern over wedge, and b) pressure coefficient on midplane of wedge with $\alpha = 15$ deg for nozzle pressure ratio $NPR = 1.2$. From [15].

$$Sr = \frac{fd_j}{u_j} = 0.5$$

which is near the peak value for noise from fine-scale turbulence emitted by turbulent jets. Assuming that this relation holds for the fine (woven-mesh) perforation, the fine-perforation flaps produced noise at full-scale frequencies ranging from 3.1 to 7.8 kHz, depending on whether one uses the long or short side of the perforation (these frequencies were not resolved in the experiment). For a full-scale application, a perforation of 10-mm-diam circular holes is expected to generate sound at 7.0 kHz, which gets attenuated very rapidly by atmospheric absorption. For example, at conditions of least absorption (temperature of 30°C, relative humidity of 70%), the predictions by Bass et al. [18] indicate that sound at 3 kHz is attenuated by 17 dB per km, whereas sound at 7 kHz is attenuated by 49 dB per km.

V. Mean-Velocity Field

A. Near-Field Profiles

The presence of the pylon prevented full 3-D mapping of the velocity field very close to the nozzle using the pitot rake. However, localized surveys very close to the nozzle were possible by limiting the motion of the probe to only one direction. Of interest here was the flow immediately downstream of the flap. The top probe of the pitot rake was positioned 5 mm downstream of the exit of the core nozzle (10 mm downstream of the flap trailing edge). The path of the probe and resulting pitot pressure and velocity profiles are shown in Fig. 19 for the baseline case, the case with solid flaps, and the case with fine-perforation flaps.

The profiles for the baseline case are straightforward and illustrate clearly the regions of primary (core) and secondary (fan) flows. The profiles for the solid flaps show two important phenomena. First, the pressure differential behind the flap becomes negative. In this stagnant region, the pitot probe acts like a static-pressure probe. The minimum pressure differential is -0.42 psig, which corresponds to $C_p = -0.1$. This is of the same order as the experimental value of the base pressure coefficient measured in the large-scale experiment of Papamoschou et al. [15] (Fig. 18b). Second, there is a high-velocity

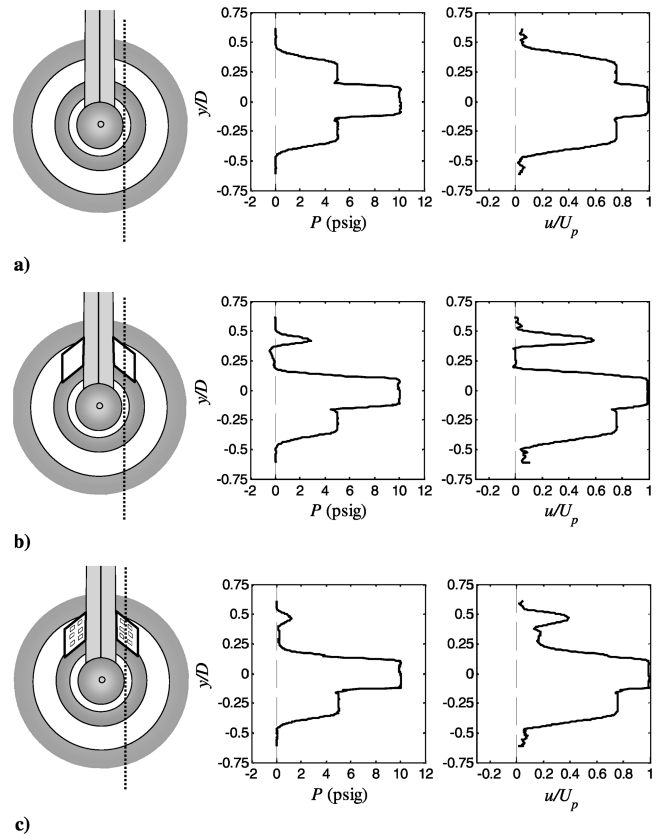


Fig. 19 Near-field pitot pressure and velocity profiles (dashed blue line indicates path of pitot probe): a) baseline, b) solid flaps, and c) perforated flaps (fine mesh).

spike directly above the flap, probably caused by the upwash of the fan flow over the side of the flap (Fig. 18a). The strong gradients associated with the velocity spike could be an additional source of noise generation. The flow behind the perforated flaps is different.

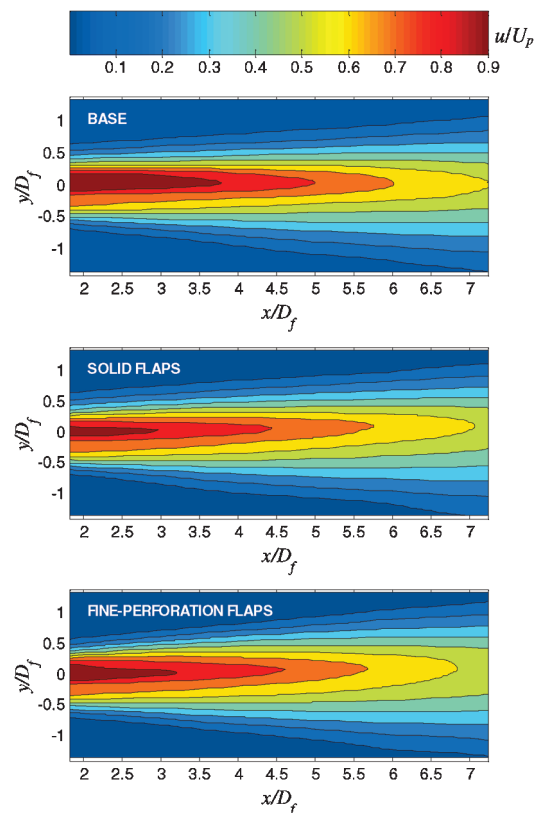


Fig. 20 Isocontours of u/U_p on the $z = 0$ (symmetry) plane.

First, there is a small positive pitot pressure behind the flap. The corresponding velocity is 23% of the fan exit velocity. The measurement of a finite velocity behind the flap indicates that the base pressure coefficient is practically zero, which correlates with our expectation that the perforated flaps have less drag than the solid flaps. Second, the velocity excess above the flap is much smaller than for the solid flap. It is evident from Fig. 19 that the perforation reduced substantially the velocity gradients in the region immediately downstream of the flap.

B. Mean-Flow Mapping

This section presents the full 3-D mapping of the mean-velocity field and its first and second radial derivatives. Profiles start at $x/D_f = 1.7$, and so small-scale details seen in the near-field profiles are likely to be smeared out or dissipated by that station. For each axial station, the radial derivatives are calculated on the radial-azimuthal ($r-\phi$) coordinate system. The origin of the $r-\phi$ plane is defined as the centroid of the region where the pitot pressure exceeds 95% of its maximum value. The first and second derivatives are calculated along radial lines from $\phi = -178$ to 180 deg in increments of 2 deg. The derivative values on the $r-\phi$ plane are then interpolated on the Cartesian $y-z$ plane. The radial velocity gradient is presented in the normalized form

$$\frac{D_f}{U_p} \frac{\partial u}{\partial r}$$

Isocontours of the mean axial velocity u , normalized by the core velocity U_p , on the symmetry plane $z = 0$ are shown in Fig. 20. The base flow is asymmetric due to the presence of the pylon. The pylon flaps enhance this asymmetry but in subtle ways not readily apparent in these plots. One feature that is clear, though, is that the deflectors reduce the extent of the high-speed region. The primary potential-core length, defined here as the length of the $u/U_p = 0.9$ level, is reduced from $x/D_f = 3.5$ to $x/D_f = 2.7$ (23%) using the solid flaps and to $x/D_f = 2.9$ (17%) using the fine-perforation flaps. In addition, both types of flaps reduce the radial extent of the high-speed region. This will become more evident in subsequent figures.

Figure 21 plots isocontours of $u(x_0, y, z)/U_p$ for various axial stations x_0 . We note again that the baseline flow is not axisymmetric because of the presence of the pylon. The baseline profiles are pear-shaped with moderately thicker fan flow below the core flow. This distortion from axial symmetry does not evolve appreciably with downstream distance. In contrast, the profiles for the jets with flaps distort into more vertically oblong shapes with downstream distance, with significant thickening of the low-speed flow underneath the core jet. Interestingly, the perforated flaps create more distortion than the

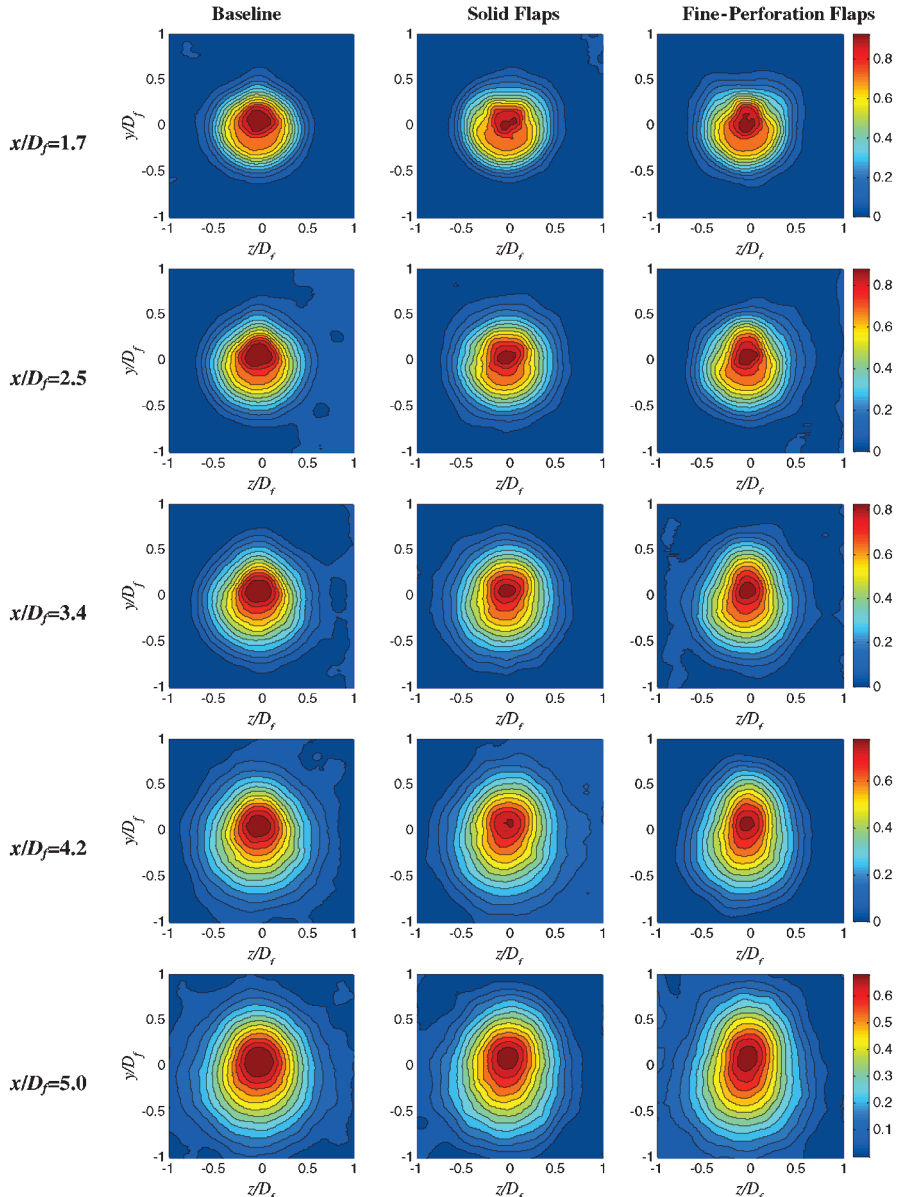


Fig. 21 Isocontours of u/U_p on various x planes.

solid flaps far downstream of the nozzle. Importantly, both types of flaps reduce the extent of the high-speed region and thus compact the noise sources closer to the nozzle.

The contours of radial velocity gradient, plotted in Fig. 22, show important features not easily discernible from the velocity profiles. The baseline jet has strong velocity gradients near the extended location of the pylon, on the top side of the jet. Surprisingly, the flaps reduce these gradients, a significant departure from wedges installed on axisymmetric nozzles. It is important to note that the high-gradient region for the baseline flow in Fig. 22 coincides with the region of noise-source generation in the computational studies of Hunter et al. [9]. On the lower side of the jet, the flaps reduce the peak velocity gradient for $x/D_f > 4.2$. The gradient maps show slight asymmetry around the nozzle centerplane, the result of minute departures from symmetry in the alignment of the nozzle components and pylon. Previous works have noted how difficult is it to have a perfectly symmetric exhaust from a dual-stream nozzle [8,10]. Considering the asymmetries observed in past large-scale tests of similar nozzle–pylon configurations [10], the present asymmetries are deemed very minor and thus unlikely to impact the results of this study.

The maps of the second radial derivative of the mean velocity allow location of the inflection points of the velocity profile on the r - ϕ plane. As discussed in the Introduction (Fig. 1), the locus of the outer inflection points i_2 and i_3 defines the region where the core jet is silenced by the fan flow. Figure 23 shows the locus of the inflection points and highlights by light green color the area enclosed by the lines i_2 and i_3 . Also plotted, in red, is the high-speed region of the flow defined by $u \geq 0.8U_p$. In simple terms, one can think of the red region as the core noise-source region and the green inflectional layer as a “fluid shield” that silences the core noise sources. The greater the extent of the inflectional layer, in relation to the noise-source region, the stronger the potential for noise reduction. The azimuthal extent of the inflectional layer may indicate which azimuthal directions are best treated using this approach. It is evident by the plots of Fig. 23 that both types of flaps cause more extensive inflectional layers. In addition, as noted earlier, both types of flaps compact the high-speed region. By $x/D_f = 4.2$, the baseline jet loses almost completely its inflectional layer but still has an appreciable high-speed region. In contrast, the jets with flaps retain a noticeable inflectional layer and their high-speed region is practically vanished. The biggest advantage occurs past $x/D_f = 3.8$, consistent with the noise-source

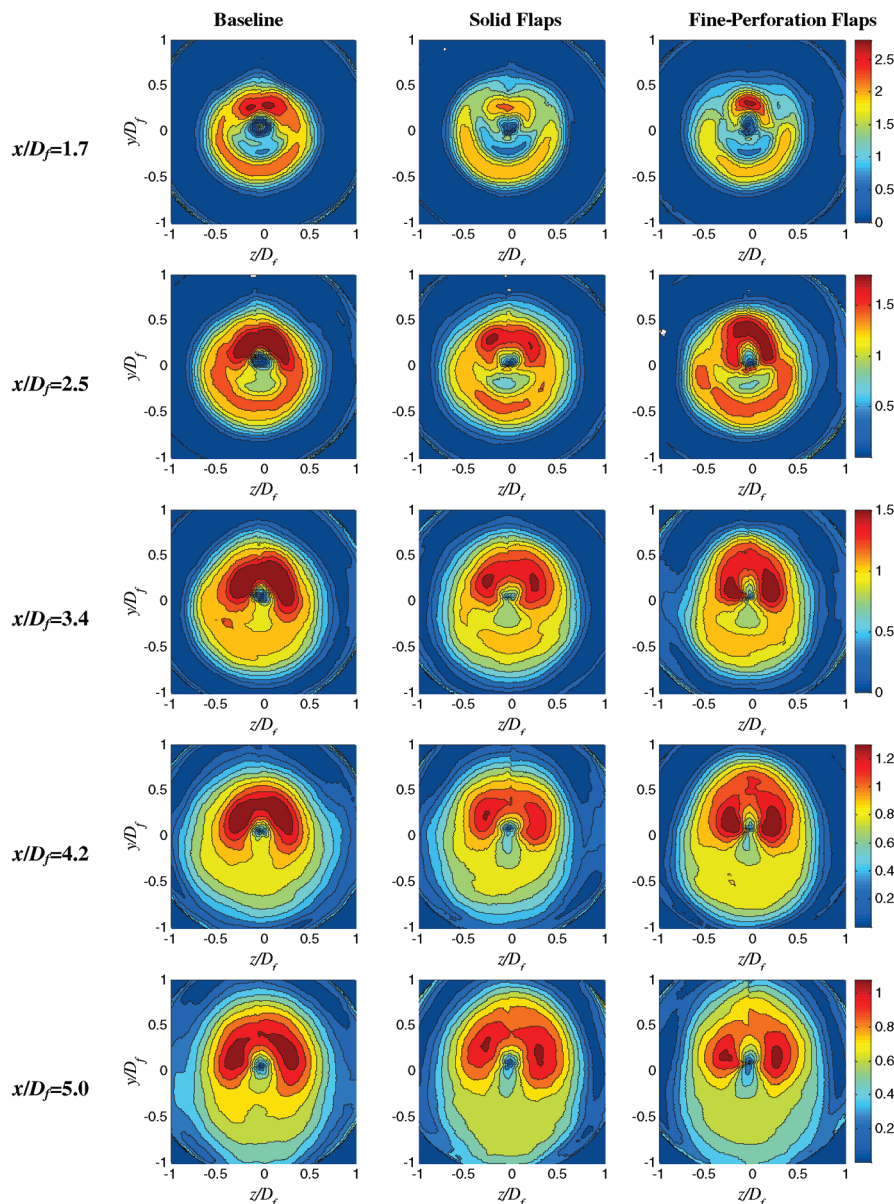


Fig. 22 Isocontours of radial velocity gradient on various x planes.

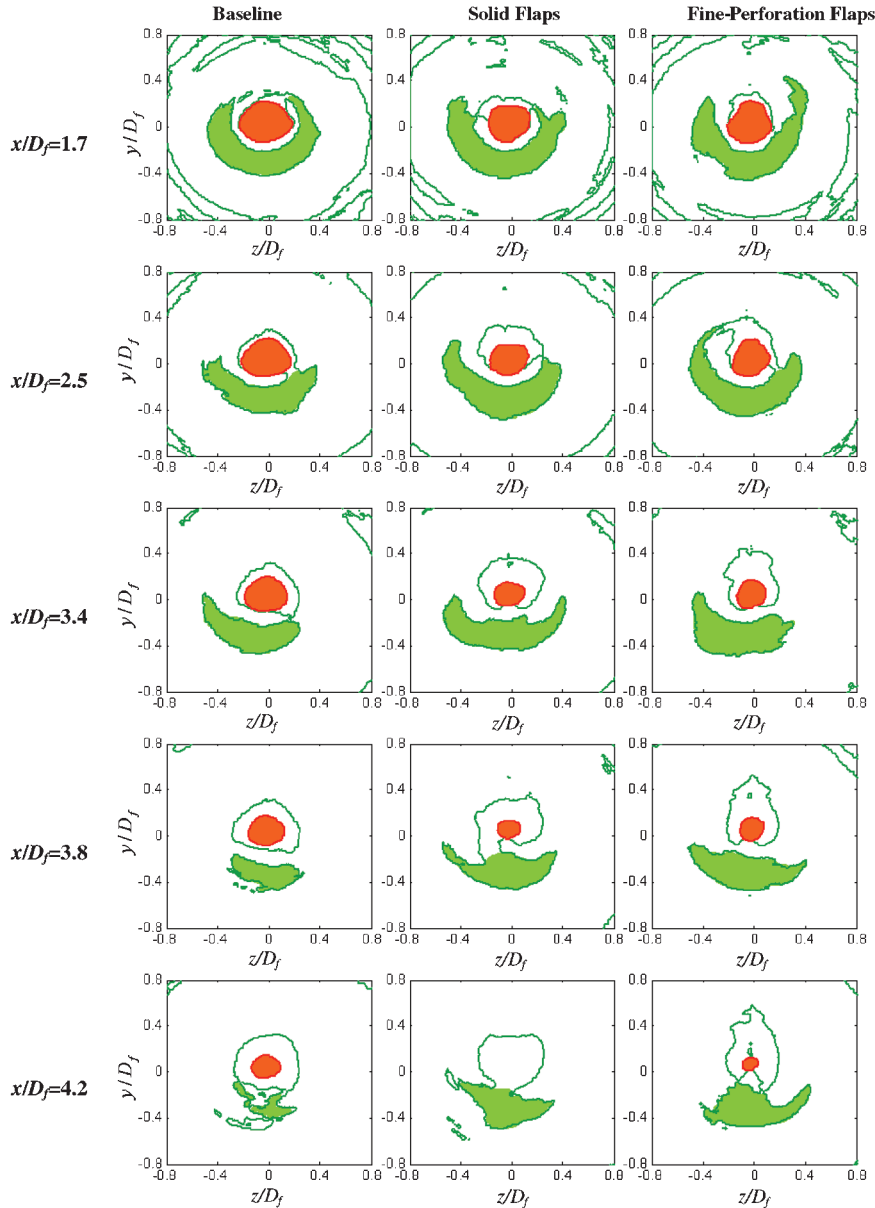


Fig. 23 Inflectional layer and high-speed region on several x planes.

reduction seen in the maps of Figs. 16 and 17. Overall, the inflectional layer is thicker at $\phi = 0$ deg than at $\phi = 60$ deg, which may explain the better noise reduction at $\phi = 0$ deg noted in Sec. III.

VI. Conclusions

This experimental investigation examined the potential of pylon-mounted flap deflectors to reduce jet noise of separate-flow turbofan engines with a bypass ratio of eight. The main function of the deflectors is to thicken the low-speed region surrounding the core jet in the downward and sideline directions. The study encompassed acoustic measurements, noise-source imaging, mean-velocity surveys, and aerodynamic estimates. Three types of deflectors were tested: solid flaps, porous flaps made of coarse perforation, and porous flaps made of fine perforation. The porosity was about 50% for both coarse- and fine-perforation flaps. The deflection angle was 22 deg for all the flaps.

The baseline flow is nonaxisymmetric due to the presence of the pylon. The baseline flowfield includes a moderately thickened flow on the bottom side of the jet and strong velocity gradients at the top of the jet. It is shown that all the deflectors reduce noise sources near the end of the primary potential core. The reduction is strongest for sources emitting sound in the aft quadrant but remains appreciable

for sources emitting sound at large polar angles from the jet exit. Mechanisms of the noise reduction involve elongation of the secondary inflectional layer on the lower side of the jet, in combination with a compaction of the high-speed region and reduced velocity gradients past the end of the potential core.

The solid flaps create excess noise in the vicinity of their location that can overwhelm the noise benefit, particularly at large polar angles and azimuth angles that allow direct line of sight of the flaps. It is noted that the excess noise is particularly strong for the relatively large flap angle (22 deg) used here. Flaps with smaller angles produce less excess noise. Nevertheless, it is important to understand and cure this undesirable feature of wedge- and flap-type deflectors. Likely sources of the excess noise are the increased shear on the top of the jet, caused by the dead region behind the flap, and a strong velocity spike on the top of the flap, caused by the upwash of the fan flow over the surface of the flap. Perforated flaps mitigate both of these adverse effects and reduce substantially the resulting excess noise. However, the perforations themselves can cause noise at high frequency. It is shown that this noise can be moved to very high frequency (rapidly attenuated by atmospheric absorption) by reducing the size of the perforation. Accordingly, the fine-perforation flaps provided superior acoustic results yielding EPNL benefits of 2.1 dB in the downward direction and 1.0 dB in the sideline direction.

A surprising result is that the flaps reduce the velocity gradients, created by the pylon, on the top of the jet. This is opposite to the trends observed when wedges or flaps were installed in axisymmetric nozzles. The gradient reduction may have beneficial impacts on upward-emitted noise that reflects from the wing surface.

Acknowledgment

The authors thank An Vu for his CAD design of the slotted pylon. The noise suppression method of pylon deflectors is proprietary to the University of California; U.S. Patent Pending.

References

- [1] Papamoschou, D., "Fan Flow Deflection in Simulated Turbofan Exhaust," *AIAA Journal*, Vol. 44, No. 12, 2006, pp. 3088–3097. doi:10.2514/1.22552
- [2] Papamoschou, D., "New Method for Jet Noise Suppression in Turbofan Engines," *AIAA Journal*, Vol. 42, No. 11, 2004, pp. 2245–2253. doi:10.2514/1.4788
- [3] Fisher, M. J., Preston, G. A., and Bryce, W. D., "A Modelling of the Noise from Simple Coaxial Jets, Part 1: With Unheated Primary Flow," *Journal of Sound and Vibration*, Vol. 209, No. 3, 1998, pp. 385–403. doi:10.1006/jsvi.1997.1218
- [4] Zaman, K. B. M. Q., and Papamoschou, D., "Effect of a Wedge on Coannular Jet Noise", AIAA Paper 2006-0007, Jan. 2006.
- [5] Zaman, K. B. M. Q., Bridges, J., and Papamoschou, D., "Offset Stream Technology: Comparison of Results from UCI and GRC," AIAA Paper 2007-0438, Jan. 2007.
- [6] Shupe, R. S., Zaman, K. B. M. Q., and Papamoschou, D., "Effect of Wedge-Shaped Deflectors on Flow Fields of Dual-Stream Jets," AIAA Paper 2007-3659, May 2007.
- [7] Bridges, J. E., and Wernet, M. P., "Effect of Temperature on Jet Velocity Spectra," NASA TM 2007-214993, Oct. 2007.
- [8] Viswanathan, K., "Does a Model-Scale Nozzle Emit the Same Jet Noise as a Jet Engine?" *AIAA Journal*, Vol. 46, No. 2, 2008, pp. 336–355. doi:10.2514/1.18019
- [9] Hunter, C. A., Thomas, R. H., Abdol-Hamid, K. S., Pao, S. P., Elmiligui, A. A., and Massey, S. J., "Computational Analysis of the Flow and Acoustic Effects of Jet-Pylon Interaction," AIAA Paper 2005-3083, May 2005.
- [10] Birch, S. F., Khritov, K. M., Maslov, V. P., Mironov, A. K., and Secundov, A. N., "An Experimental Study of Flow Asymmetry in Co-axial Jets," AIAA Paper 2005-2845, May 2005.
- [11] Papamoschou, D., "Imaging of Distributed Directional Noise Sources," AIAA Paper 2008-2885, May 2008.
- [12] Brooks, T. F., and Humphreys, W. M., "A Deconvolution Approach for the Mapping of Acoustic Sources (DAMAS) Determined from Phased Microphone Arrays," *Journal of Sound and Vibration*, Vol. 294, Nos. 4–5, 2006, pp. 856–879. doi:10.1016/j.jsv.2005.12.046
- [13] Savitzky, A., and Golay, M. J. E., "Smoothing and Differentiation of Data by Simplified Least Squares Procedures," *Analytical Chemistry*, Vol. 36, No. 8, 1964, pp. 1627–1639. doi:10.1021/ac60214a047
- [14] Liepmann, H. W., and Roshko, A., *Elements of Gas Dynamics*, Wiley, New York, 1957, p. 148.
- [15] Papamoschou, D., Vu, A., and Johnson, A., "Aerodynamics of Wedge-Shaped Deflectors for Jet Noise Reduction," AIAA Paper 2006-3655, June 2006.
- [16] Castro, I. P., "Wake Characteristics of Two-Dimensional Perforated Plates Normal to an Airstream," *Journal of Fluid Mechanics*, Vol. 46, Pt. 3, 1971, pp. 599–609. doi:10.1017/S0022112071000727
- [17] Sakaliyski, K. D., Hileman, J. I., and Spakovzky, Z. S., "Aero-Acoustics of Perforated Drag Plates for Quiet Transportation Aircraft," AIAA Paper 2007-1032, Jan. 2007.
- [18] Bass, H. E., Sutherland, L. C., Zuckerwar, A. J., Blackstock, D. T., and Hester, D. M., "Atmospheric Absorption of Sound: Further Developments," *Journal of the Acoustical Society of America*, Vol. 97, No. 1, 1995, pp. 680–683. doi:10.1121/1.412989

C. Bailly
Associate Editor